第 50 卷 第 22 期/2023 年 11 月/中国激光 研究论文

中国激光

超快激光X射线单发照相的图像增强方法研究

唐立平[1,2]，王窈[3]，储根柏[4]，李奉笑[1,2]，王亮[3]，周日峰[1,2*]，何碧[3**]

[1]重庆大学光电技术及系统教育部重点实验室ICT研究中心，重庆 400044；
[2]重庆大学工业CT无损检测教育部工程研究中心，重庆 400044；
[3]中国工程物理研究院化工材料研究所，四川 绵阳 621900；
[4]中国工程物理研究院激光聚变研究中心高温高密度等离子体物理实验室，四川 绵阳 621900

摘要 超快激光X射线单发照相技术具有高时空分辨能力，是观测高速运动物体形态参数如内部结构、平面性等的重要手段。但由于激光X射线脉宽在皮秒或飞秒量级、X射线能谱宽、成像环境复杂等原因，导致X射线图像背景干扰噪声大、对比度低，物体形态结构准确识别和测量难度大。在传统对比度限制直方图均衡化(CLAHE)图像增强算法的基础上，提出了一种多尺度融合的改进直方图均衡化(IHEMF)算法。该算法增加自适应裁剪阈值以适应每个区域特征，并利用亮度和梯度幅值信息将增强后图像与原始图像全局融合，最后对融合后图像去噪得到最终图像。该算法既能提高感兴趣区域的对比度噪声比(CNR)，又具有很好的保边界特征的能力。对高速飞片的静态、动态、终态等典型状态下X射线图像进行处理，CNR分别提升50.97%、90.43%和96.84%。实验结果表明所提算法在噪声抑制和结构保真方面优于其他算法，可为准确解读高速运动物体形态表征参数信息提供重要技术支撑。

关键词 超快激光；X射线单发照相；图像增强；多尺度融合；直方图均衡化

中图分类号 TP391.41 **文献标志码** A **DOI:** 10.3788/CJL230486

1 引 言

因超快激光驱动产生的X射线通量高、焦斑小，超快激光X射线单发照相技术能对超高速度物体进行高时空分辨X射线成像，为观测高速运动物体形态参数如飞片内部结构、平面性等提供了新的技术手段[1-4]。但激光打靶产生的高能X射线的能谱范围宽，并且伴随高能电子、杂散射线等强干扰，对X射线成像信噪比和图像质量造成了很大的干扰。同时，激光X射线脉宽极窄(皮秒或飞秒量级)，辐射探测器的数据采集时间极短，导致光子数少，量子统计噪声大[5]，图像信噪比低。另外，结构复杂的高密度金属对X射线的散射使得图像的背景干扰大、对比度噪声比(CNR)低。并且飞片周围等离子体[6-8]使得观察飞片结构更加困难，图像质量难以满足精确观测的应用要求。为更好地观察和分析物体的形态结构，需要针对超快激光X射线单发照相装置及其成像特点，采用特殊的图像增强算法以提升图像质量。

关于X射线图像增强问题，国内外学者做了许多研究工作，其中直方图、Retinex等理论应用比较广泛[9-11]。直方图均衡化(HE)算法由于原理简单、计算量小等优点，被广泛应用于各种图像增强任务。但由于直方图的扁平化特性，存在灰度级合并现象，在高动态范围图像上表现为细节丢失[12]。亮度保持双直方图均衡化(BBHE)算法以图像均值为阈值将图像划分为两个子图分别增强，可以有效地保留图像亮度信息和减少灰度级丢失，但单一阈值难以满足每个灰度范围内的细节增强[13-15]。对比度限制双边直方图均衡化(cl-BHE)算法以固定间隔的灰度阈值将图像分为若干子图像并使用双边滤波对加权矩阵滤波，抑制了图像增强过程中的振铃伪影，但有用信息被放大的噪声淹没[16]。对比度限制直方图均衡化(CLAHE)算法通过限制局部直方图的高度，在改善对比度的同时削弱了噪声过度放大，但在明暗分界处存在光晕[17-21]。模糊上下文对比度增强(FCCE)算法引入模糊隶属函数来表征像素的邻域性质，并开发了模糊不相似度直方图，有效地保留物体的结构且不引入人工伪影，但对于X射线图像存在亮度增强不足的问题[22]。Retinex理论通过消除光照分量增强图像对比度，但其相关算法建立在光照分量平滑假设的基础上，在明暗边界处易引入伪影[23-25]。总之，尽管直方图、Retinex等理论得到了广泛应用，但直接应用于超快激光单发X射线图像仍存在细节丢失、噪声放大、人工伪影等不足。

针对这一问题，本文提出一种多尺度融合的改进

收稿日期：2023-02-02；**修回日期**：2023-02-27；**录用日期**：2023-03-15；**网络首发日期**：2023-03-23

基金项目：国家自然科学基金面上项目(12175026)、国家自然科学基金重大科研仪器研制项目(11827809)

通信作者：*zhou65112401@cqu.edu.cn；**hebi@caep.cn

直方图均衡化(IHEMF)算法。该算法通过增加裁剪阈值函数实现了区域自适应增强;同时,利用亮度和梯度幅值信息将自适应增强后图像与原始图像全局融合,解决了明暗边界增强时引入人工伪影的问题;最后通过三维块匹配(BM3D)算法去除量子统计噪声和大量等离子干扰,得到增强图像。理论上,该算法能在保留细节特征的同时提高感兴趣区域对比度,大幅提升图像质量,为准确解读高速运动物体形态表征参数信息提供重要技术支撑。

2 单发X射线照相方法简介

超快激光X射线单发照相技术主要采用大能量皮秒或飞秒激光作用产生微焦点、高亮度的X射线源,通过点投影成像设计,实现高时空分辨率照相。成像记录介质通常采用成像板(IP)或面阵电荷耦合器件(CCD)探测器,像素单元尺寸为数十微米,提高成像的空间分辨率。记录介质前放置滤片以滤掉低能X射线,使得能量合适的X射线到达记录介质并提高成像质量。通常采用阶梯楔形的密度校准块,标定成像物体的密度。照相技术原理如图1所示,大能量皮秒或飞秒激光轰击金属靶材,通常使用丝靶提高分辨率,以产生微焦斑、高亮度强X射线源,X射线穿过高速运动物体后被记录介质接收并输出X射线图像。动态实验被测对象是高速运动的物体,本文中采用的是小尺寸高速飞片,获得的动态图像用于解读飞片的内部结构、平面性等形态参数。动态实验前后分别开展静态实验,实验前测量飞片材料图像以表征单发成像的图像质量,实验后测量飞片产生后剩余材料以分析动态过程。下面,实验前、中、后的X射线图像用静态图像、动态图像、终态图像表述。

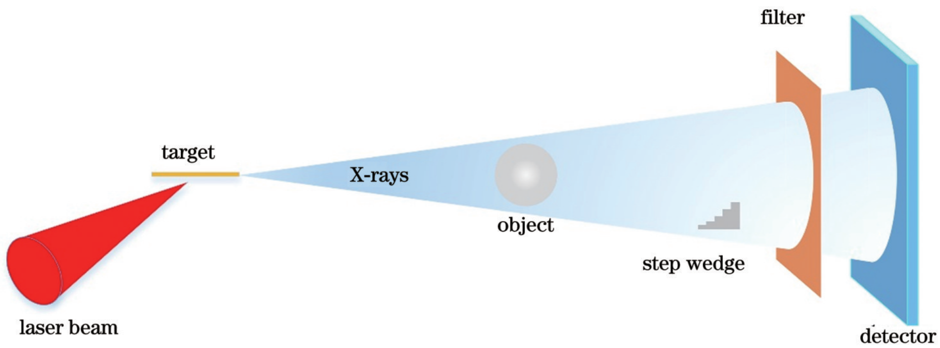

图1 超快激光X射线单发照相原理

Fig. 1 Schematic of single-shot X-ray radiograph via ultrafast laser

3 图像增强算法

常规CLAHE算法的关键是通过裁剪直方图来控制对比度放大的程度,利用预先给定的阈值对直方图进行裁剪。超过阈值的像素将会被重新平均地分配到每个灰度级上,实现增强。裁剪阈值的取值影响图像的增强程度,其值越大,增强效果越强。当对比度过低时,必须将裁剪阈值设置得非常大。由于裁剪阈值是预先给定的且图像各子块的限制幅度是相对一致的,没有反映出背景区域和感兴趣区域的区别,导致背景区域过度增强。

因此,提出改进直方图(IHE)算法,增加自适应裁剪阈值以适应每个区域特征。另外,由于金属腔高密度材料对X射线的强吸收导致腔边缘与空气的对比度很强,CLAHE算法处理后,在对比强烈的腔边缘区域会产生光晕。因此提出IHEMF算法,算法流程如图2所示。IHEMF算法结合IHE和多尺度融合(MF)算法:首先使用IHE算法对原始图像自适应增强得到增强后图像;再利用亮度和梯度幅值信息将IHE增强图像与原始图像全局融合得到融合后图像,抑制光晕和块效应并提高边界保持能力;最后采用BM3D减小等离子体和量子统计噪声对飞片结构的干扰,得到最终图像。

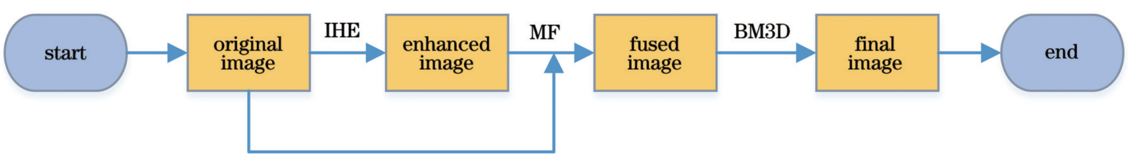

图2 IHEMF算法流程图

Fig. 2 Flow chart of IHEMF algorithm

3.1 IHE增强算法

IHE算法核心思想是对CLAHE算法的直方图裁剪阈值进行校正,每个子块的裁剪阈值与局部梯度相关,算法流程如下。

(1) 将输入图像划分为 $m \times n$ 个连续且互不重叠的固定子块,并统计每个子块的直方图分布。

(2) 计算自适应裁剪阈值 $\boldsymbol{N}_c$:

$$N_{\mathrm{avg}}=\frac{N_x \times N_y}{L}, \tag{1}$$

$$\boldsymbol{N}_{\mathrm{c}i}=N_{\mathrm{avg}} \times\left[1+C_{\mathrm{limit}} \times \exp \left(\boldsymbol{G}_{\mathrm{e}i}\right)\right], 1 \leqslant i \leqslant m \times n, \tag{2}$$

$$\boldsymbol{G}_{\mathrm{e}i}=-\ln \left[C_{\mathrm{limit}} \times\left(\frac{\boldsymbol{G}_i-\boldsymbol{G}_{\mathrm{M}i}}{\boldsymbol{G}_{\mathrm{m}i}-\boldsymbol{G}_{\mathrm{M}i}}\right)^2\right], \tag{3}$$

$$\boldsymbol{G}_i=\sqrt{\boldsymbol{g}_{xi}^2+\boldsymbol{g}_{yi}^2}, \tag{4}$$

式中：N_x和N_y分别为子块水平和垂直方向的像素个数；L为最大灰度级数（本文中L取值为65536）；N_{avg}为每个灰度级分到的平均像素数；C_{limit}为裁剪系数；$\boldsymbol{N}_{\mathrm{c}}$为自适应裁剪阈值矩阵；$\boldsymbol{N}_{\mathrm{c}i}$为第$i$个图像块的裁剪阈值；$\boldsymbol{G}$为图像子块梯度矩阵；$\boldsymbol{G}_{\mathrm{M}i}$和$\boldsymbol{G}_{\mathrm{m}i}$分别为$\boldsymbol{G}_i(1 \leqslant i \leqslant m \times n)$的均值和最小值；$\boldsymbol{g}_x$和$\boldsymbol{g}_y$分别为水平和垂直方向的梯度。

使用中值滤波对$\boldsymbol{N}_{\mathrm{c}}$做平滑处理，防止阈值差异过大出现块效应。

（3）裁剪各个子块的直方图并重新分配裁剪的像素，得到裁剪后的直方图：

$$N_{\mathrm{e}}=\sum_{i=1}^{L-1}\left\{\max \left[\boldsymbol{H}(i)-\boldsymbol{N}_{\mathrm{c}i}, 0\right]\right\}, \tag{5}$$

$$N_{\mathrm{eavg}}=\frac{N_{\mathrm{e}}}{L}, \tag{6}$$

$$\hat{\boldsymbol{H}}(i)=\begin{cases}\boldsymbol{N}_{\mathrm{c}}+N_{\mathrm{eavg}}, & \boldsymbol{H}(i) \geqslant \boldsymbol{N}_{\mathrm{c}} \\ \boldsymbol{H}(i)+N_{\mathrm{eavg}}, & \boldsymbol{H}(i)<\boldsymbol{N}_{\mathrm{c}}\end{cases}, \tag{7}$$

式中：$\boldsymbol{H}(i)$为子块的直方图；N_{e}为裁剪后的像素；N_{eavg}为重新分配的平均像素；$\hat{\boldsymbol{H}}(i)$为分配后的直方图。

（4）插值并映射。若直接用子块直方图$\hat{\boldsymbol{H}}(i)$映射，增强后的图像必然出现块效应，必须对其插值处理。根据子块的位置不同，采用不同的插值算法：当子块位于图像4个角点时，不进行插值；当子块位于图像边缘且不为角点时，采用线性插值；当子块位于图像内部时，采用双线性插值（见图3）。插值公式为

$$f(x, y)=\frac{\left(x_2-x\right)\left(y_2-y\right)}{\left(x_2-x_1\right)\left(y_2-y_1\right)} f\left(Q_{11}\right)+\frac{\left(x-x_1\right)\left(y_2-y\right)}{\left(x_2-x_1\right)\left(y_2-y_1\right)} f\left(Q_{21}\right)+\frac{\left(x_2-x\right)\left(y-y_1\right)}{\left(x_2-x_1\right)\left(y_2-y_1\right)} f\left(Q_{12}\right)+\frac{\left(x-x_1\right)\left(y-y_1\right)}{\left(x_2-x_1\right)\left(y_2-y_1\right)} f\left(Q_{22}\right), \tag{8}$$

式中：(x_1, y_1)、(x_2, y_1)、(x_1, y_2)和(x_2, y_2)分别为像素P的4个相邻子块Q_{11}、Q_{21}、Q_{12}和Q_{22}的中心坐标；$f(Q_{11})$、$f(Q_{21})$、$f(Q_{12})$和$f(Q_{22})$分别为4个相邻子块的裁剪直方图映射出的新值。多个新值插值后即可得到增强后P像素值$f(x, y)$。

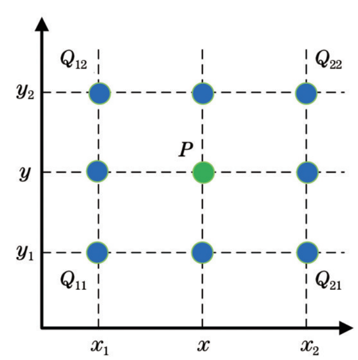

图3 双线性插值坐标示意图

Fig. 3 Diagram of bilinear interpolation

3.2 MF图像融合

由于X射线图像尺寸一般很大，子块数量m和n较小，IHE算法在明暗对比强烈的区域会产生光晕和块效应。通过将原始图像和IHE增强后的图像全局融合，来抑制光晕和块效应。算法流程如下。

（1）计算亮度权重$\boldsymbol{W}_1$：

$$\boldsymbol{W}_{1i}=-0.5 \exp \left(\frac{\boldsymbol{I}_i+\boldsymbol{I}_{\mathrm{m}i}-\boldsymbol{I}_{\mathrm{M}i}}{\sigma^2}\right), 1<i<N, \tag{9}$$

式中：$\boldsymbol{I}$为输入图像矩阵；$\boldsymbol{I}_{\mathrm{m}}$为最大灰度值矩阵；$\boldsymbol{I}_{\mathrm{M}}$为灰度均值矩阵；$\sigma$为衰减参数；$N$为输入的图像数目。

（2）计算梯度权重$\boldsymbol{W}_2$：

$$\boldsymbol{g}_{xxi}=\left|\frac{\partial \boldsymbol{I}_i}{\partial x}\right|^2, \boldsymbol{g}_{yyi}=\left|\frac{\partial \boldsymbol{I}_i}{\partial y}\right|^2, \boldsymbol{g}_{xyi}=\frac{\partial \boldsymbol{I}_i}{\partial x} \times \frac{\partial \boldsymbol{I}_i}{\partial y}, 1<i<N, \tag{10}$$

$$\theta_i=0.5 \arctan \left(\frac{2 \boldsymbol{g}_{xyi}}{\boldsymbol{g}_{xxi}-\boldsymbol{g}_{yyi}}\right), \tag{11}$$

$$\boldsymbol{W}_{2i}=0.5\left(\boldsymbol{g}_{xxi}+\boldsymbol{g}_{yyi}\right)+0.5\left(\boldsymbol{g}_{xxi}-\boldsymbol{g}_{yyi}\right) \cos 2\theta_i+\boldsymbol{g}_{xxi} \sin 2\theta_i。 \tag{12}$$

（3）计算总权重$\boldsymbol{W}$：

$$\boldsymbol{W}=\boldsymbol{W}_1^{\lambda_1}+\boldsymbol{W}_2^{\lambda_2}, \tag{13}$$

式中：λ_1和λ_2为权重调节参数。

（4）重构融合图像：

$$\boldsymbol{I}_j=\boldsymbol{I}_j+\boldsymbol{W}_{ij} \cdot \boldsymbol{P}_{ij}, 1<i<N, 1 \leqslant j \leqslant L_{\mathrm{p}}, \tag{14}$$

$$\hat{\boldsymbol{I}}=\mathrm{R}\left(\boldsymbol{I}_j\right), \tag{15}$$

式中：$\boldsymbol{W}_{ij}$为高斯金字塔分解矩阵；$\boldsymbol{P}_{ij}$表示第i张输入图像的第j层拉普拉斯金字塔分解矩阵；L_{p}为金字塔分解层数；$\boldsymbol{I}_j$为第j层加权图像；R(·)表示拉普拉斯金字塔图像重构操作[26-27]；$\hat{\boldsymbol{I}}$为重构出的融合图像。

4 实验结果

4.1 定性评价

为了验证IHEMF算法的有效性，选取静态、动态

和终态[图 4(a)、图 5(a)和图 6(a)]三种典型的超快激光单发 X 射线图像进行性能评估。选取 HE、CLAHE、多尺度 Retinex(MSR)、cl-BHE、面向反射的概率均衡化(ROPE)、FCCE 六种先进算法与 IHEMF 进行对比实验，实验环境为 i7-9700 处理器，32 GB 内存。IHEMF 算法中裁剪系数越大，图像增强效果越强，结构相似性越低，需要权衡对比度增强和飞片结构的保持[28-29]；权重调节参数越大，融合时相应的亮度或梯度权重占比越高[26]。本文选取实验参数设置如下：横向和纵向子块数量 $m=16$，$n=16$，裁剪系数 $C_{\mathrm{limit}}=100$，权重调节参数 $\lambda_1=1$，$\lambda_2=2.2$，衰减参数 $\sigma=0.2$。

对比实验结果如图 4～图 6 所示，图像深度均为 16 bit。图 4(a)为原始图像，图 4(b)～图 4(h)分别为 HE、CLAHE、MSR、cl-BHE、ROPE、FCCE、IHEMF 算法处理后的图像。图 5 和图 6 各图表示的意义与图 4 类似，图 5(a)和图 6(a)显示范围分别为[26000，30000]和[0，30000]，图 6(i)为 IHEMF 伪彩图。从图 4(a)、图 5(a)和图 6(a)得知，超快激光 X 射线单发照相实验中得到的原始图像对比度较低，且有等离子体和量子统计噪声干扰。其中图 4(a)受高密度金属半柱腔体影响，表现尤为明显，腔内的材料信息完全被背景淹没。实验结果表明，HE 算法对图像亮度和整

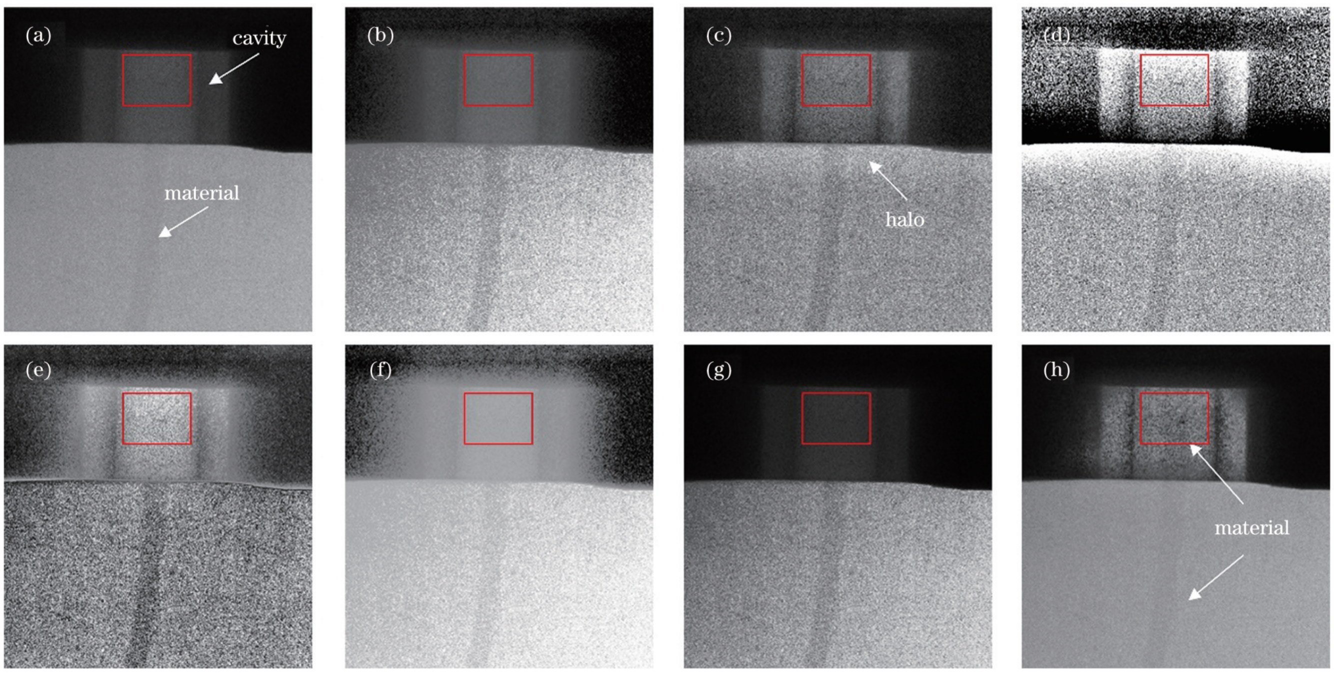

图 4　不同算法比较(静态图像)。(a)原始图像；(b)HE；(c)CLAHE；(d)MSR；(e)cl-BHE；(f)ROPE；(g)FCCE；(h)IHEMF

Fig. 4　Comparison of different algorithms (static image). (a) Original image; (b) HE; (c) CLAHE; (d) MSR; (e) cl-BHE; (f) ROPE; (g) FCCE; (h) IHEMF

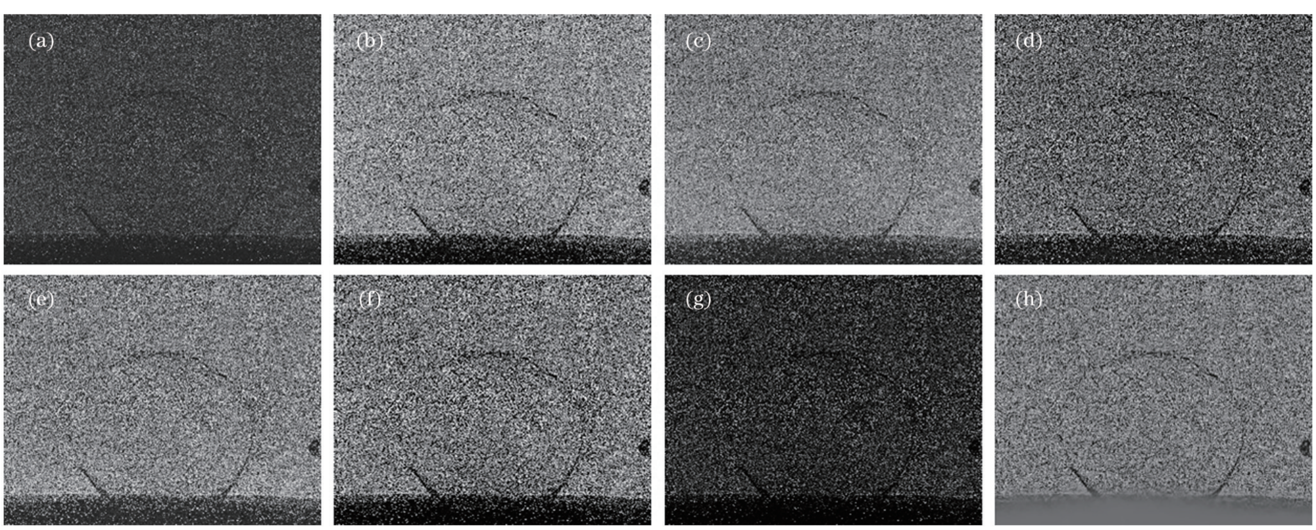

图 5　不同算法比较(动态图像)。(a)原始图像；(b)HE；(c)CLAHE；(d)MSR；(e)cl-BHE；(f)ROPE；(g)FCCE；(h)IHEMF

Fig. 5　Comparison of different algorithms (dynamic image). (a) Original image; (b) HE; (c) CLAHE; (d) MSR; (e) cl-BHE; (f) ROPE; (g) FCCE; (h) IHEMF

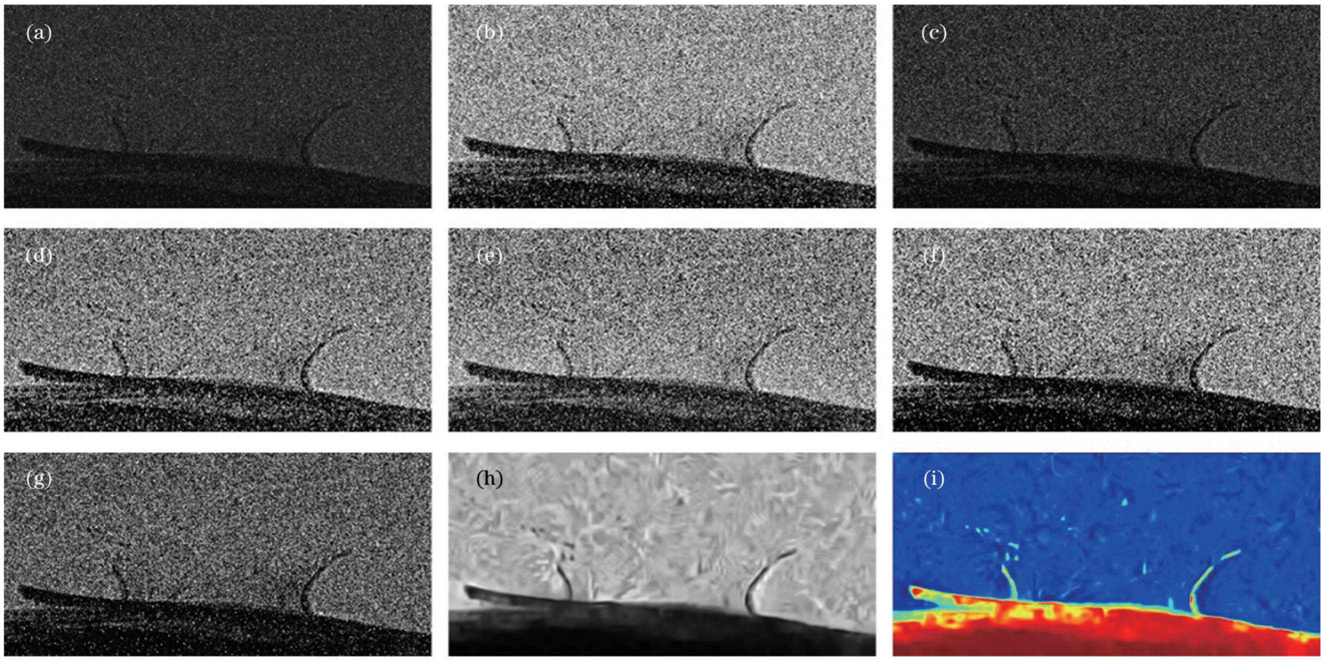

图6　不同算法比较(终态图像)。(a)原始图像;(b)HE;(c)CLAHE;(d)MSR;(e)cl-BHE;(f)ROPE;(g)FCCE;(h)IHEMF;(i)IHEMF伪彩图

Fig. 6　Comparison of different algorithms (final image). (a) Original image; (b) HE; (c) CLAHE; (d) MSR; (e) cl-BHE; (f) ROPE; (g) FCCE; (h) IHEMF; (i) pseudo-color image of IHEMF

体对比度提升明显,但某些感兴趣区域对比度效果有限,如图4(b),HE算法处理后图像未突出腔体内部材料形态。如图4(c)和图4(d)所示,CLAHE和MSR算法处理后的图像在腔体分界处产生了明显的晕圈伪影。图4(e)、图4(f)、图5(f)、图6(e)等图中,cl-BHE和ROPE算法没有根据区域特征进行增强,表现为背景过度增强。FCCE算法结构保持完整,但亮度提升不明显[图4(g)、图5(g)和图6(g)],图5(g)中飞片形态不够清晰。为满足不同区域的增强要求,IHEMF算法增加了变化的裁剪阈值,静态图像自适应裁剪阈值分布如图7所示。腔体内部的裁剪阈值比较大,背景区域阈值较小,增强感兴趣区域同时避免背景过度增强。同时,IHEMF将原始图像与IHE算法增强后图像全局融合,有效抑制了明暗边界处的光晕,增强后图像对比度显著提高,能直观分辨出物体形态[图4(h)、图5(h)和图6(h)]。

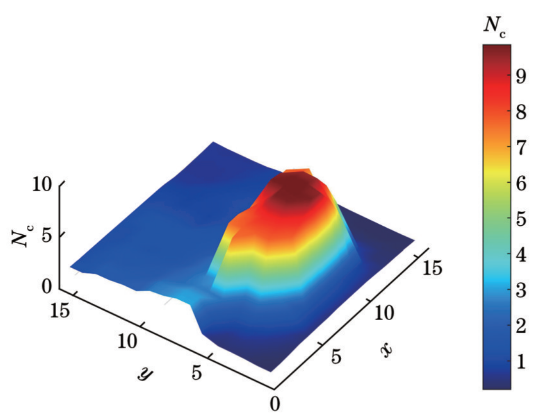

图7　静态图像的自适应裁剪阈值图

Fig. 7　Adaptive clipping threshold map of static image

4.2　定量评价

超快激光单发X射线图像增强算法是在保持图像有效信息(即内部结构、平面性等)的前提下,尽可能增强图像有效信息与图像背景的灰度差来提高图像对比度,从而实现观察物体形态的目的。图像的CNR反映了分辨图像感兴趣区域的能力[30-32],通常情况下,图像CNR越大,就越容易分辨出感兴趣区域。因此,采用图像CNR定量评估图像增强方法有效性,其计算公式如下:

$$R_{\mathrm{CNR}}=\frac{\left|\bar{N}-\bar{M}\right|}{\sqrt{\sigma_N^2+\sigma_M^2}},\tag{16}$$

式中:$\bar{N}$为有效信号(细节)区域灰度均值,σ_N^2为对应的方差;$\bar{M}$为背景区域(背景区域与有效信号区域的像素数量和形状相同)的灰度均值,σ_M^2为对应的方差。

IHEMF算法与HE、CLAHE、MSR、cl-BHE、ROPE、FCCE等几种先进算法的图像CNR对比如表1所示。从表1可以看出,MSR算法处理后CNR提升不明显,HE、CLAHE、cl-BHE、ROPE、FCCE处理后的部分图像CNR存在下降现象。IHEMF算法将图4(a)、图5(a)、图6(a)的CNR分别提升至0.311、0.179、0.622,较原始图像提升比例分别为50.97%、90.43%和96.84%,优于其他算法。CNR结果表明,IHEMF算法拥有更高的均值差($\left|\bar{N}-\bar{M}\right|$)或更低的标准差($\sigma_N^2+\sigma_M^2$),对图像CNR提升明显[33-35],与定性评价结论相符。

表1　几种不同算法的图像CNR对比

Table 1　Image CNR comparison of several different algorithms

Image	Original	HE	CLAHE	MSR	cl-BHE	ROPE	FCCE	IHEMF
Fig. 4(a)	0.206	0.042	0.231	0.289	0.196	0.130	0.053	0.311
Fig. 5(a)	0.094	0.167	0.053	0.101	0.137	0.149	0.097	0.179
Fig. 6(a)	0.316	0.392	0.281	0.337	0.301	0.366	0.316	0.622

5　结　　论

因激光打靶时产生高能电子和杂散射线、激光脉宽极窄、被测对象中高密度金属等影响，导致X射线图像噪声大、对比度低，物体形态难以识别。针对该问题，本文提出了IHEMF算法：通过引入梯度相关的自适应裁剪阈值函数，有效消除了背景区域过度增强；利用图像亮度和梯度幅值信息，将原始图像和IHE增强后图像全局融合，抑制了光晕。主观上，IHEMF处理后的图像质量更好，飞片结构清晰可辨且未引入人工伪影；客观上，与HE、CLAHE、MSR、cl-BHE、ROPE、FCCE等算法相比，IHEMF的CNR提升优于其他算法，感兴趣区域对比度更高。实验结果表明，IHEMF应用于超快激光单发X射线图像增强效果显著，为后续准确解读飞片形态表征参数信息等奠定了基础，并有利于推动超快激光X射线单发照相技术的应用。

参　考　文　献

[1] Willey T M, Champley K, Hodgin R, et al. X-ray imaging and 3D reconstruction of in-flight exploding foil initiator flyers[J]. Journal of Applied Physics, 2016, 119(23): 235901.

[2] 周维民, 于明海, 张天奎, 等. 基于皮秒拍瓦激光的高分辨X射线背光照相研究[J]. 中国激光, 2020, 47(5): 0500010.
Zhou W M, Yu M H, Zhang T K, et al. High-resolution X-ray backlight radiography using picosecond petawatt laser[J]. Chinese Journal of Lasers, 2020, 47(5): 0500010.

[3] Suzuki-Vidal F, Clayson T, Stehlé C, et al. First radiative shock experiments on the SG-II laser[J]. High Power Laser Science and Engineering, 2021, 9: e27.

[4] Li M, Yao T, Yang Z H, et al. Designing a toroidal crystal for monochromatic X-ray imaging of a laser-produced He-like plasma [J]. High Power Laser Science and Engineering, 2022, 10: e37.

[5] Chang Z Q, Zhang R Q, Thibault J B, et al. Modeling and pretreatment of photon-starved CT data for iterative reconstruction[J]. IEEE Transactions on Medical Imaging, 2017, 36(1): 277-287.

[6] Wang R R, Chen W M, Mao C S, et al. Laser-produced plasma He-alpha source for pulse radiography[J]. Chinese Optics Letters, 2009, 7(2): 156-158.

[7] 税敏, 席涛, 闫永宏, 等. 激光等离子体射流驱动亚毫米直径铝飞片及姿态诊断[J]. 物理学报, 2022, 71(9): 095201.
Shui M, Xi T, Yan Y H, et al. Laser-plasma jet driven submillimeter diameter aluminum flyer and its gesture diagnosis[J]. Acta Physica Sinica, 2022, 71(9): 095201.

[8] 储根柏, 于明海, 税敏, 等. 强激光间接驱动材料动态破碎过程的实验技术研究[J]. 物理学报, 2020, 69(2): 026201.
Chu G B, Yu M H, Shui M, et al. Experimental technique for dynamic fragmentation of materials via indirect drive by high-intensity laser[J]. Acta Physica Sinica, 2020, 69(2): 026201.

[9] Liu S X, Long W, He L, et al. Retinex-based fast algorithm for low-light image enhancement[J]. Entropy, 2021, 23(6): 746.

[10] Yakno M, Mohamad-Saleh J, Ibrahim M Z. Dorsal hand vein image enhancement using fusion of CLAHE and fuzzy adaptive gamma[J]. Sensors, 2021, 21(19): 6445.

[11] Kumar D, Solanki A K, Ahlawat A K. Luminosity control and contrast enhancement of digital mammograms using combined application of adaptive gamma correction and DWT-SVD[J]. Journal of Sensors, 2022, 2022: 4433197.

[12] Kim Y T. Contrast enhancement using brightness preserving bi-histogram equalization[J]. IEEE Transactions on Consumer Electronics, 1997, 43(1): 1-8.

[13] Wang X W, Chen L X. Contrast enhancement using feature-preserving bi-histogram equalization[J]. Signal, Image and Video Processing, 2018, 12(4): 685-692.

[14] Zhang W D, Dong L L, Zhang T, et al. Enhancing underwater image via color correction and Bi-interval contrast enhancement[J]. Signal Processing: Image Communication, 2021, 90: 116030.

[15] Tang J R, Mat Isa N A. Bi-histogram equalization using modified histogram bins[J]. Applied Soft Computing, 2017, 55: 31-43.

[16] Madmad T, De Vleeschouwer C. Bilateral histogram equalization for X-ray image tone mapping[C]//2019 IEEE International Conference on Image Processing (ICIP), September 22-25, 2019, Taipei, China. New York: IEEE Press, 2019: 3507-3511.

[17] Sahu S M, Singh A K, Ghrera S P, et al. An approach for de-noising and contrast enhancement of retinal fundus image using CLAHE[J]. Optics & Laser Technology, 2019, 110: 87-98.

[18] Sundaram M, Ramar K, Arumugam N, et al. Histogram modified local contrast enhancement for mammogram images[J]. Applied Soft Computing, 2011, 11(8): 5809-5816.

[19] Li L L, Si Y J, Jia Z H. Medical image enhancement based on CLAHE and unsharp masking in NSCT domain[J]. Journal of Medical Imaging and Health Informatics, 2018, 8(3): 431-438.

[20] Garg D, Garg N K, Kumar M. Underwater image enhancement using blending of CLAHE and percentile methodologies[J]. Multimedia Tools and Applications, 2018, 77(20): 26545-26561.

[21] Chang Y K, Jung C, Ke P, et al. Automatic contrast-limited adaptive histogram equalization with dual gamma correction[J]. IEEE Access, 2018, 6: 11782-11792.

[22] Parihar A S, Verma O P, Khanna C. Fuzzy-contextual contrast enhancement[J]. IEEE Transactions on Image Processing, 2017, 26(4): 1810-1819.

[23] Xie S J, Lu Y, Yoon S, et al. Intensity variation normalization for finger vein recognition using guided filter based singe scale retinex [J]. Sensors, 2015, 15(7): 17089-17105.

[24] Wu X M, Sun Y Q, Kimura A, et al. Reflectance-oriented probabilistic equalization for image enhancement[C]//ICASSP 2021-2021 IEEE International Conference on Acoustics, Speech and Signal Processing (ICASSP), June 6-11, 2021, Toronto, ON, Canada. New York: IEEE Press, 2021: 1835-1839.

[25] Fu Q T, Jung C, Xu K Q. Retinex-based perceptual contrast enhancement in images using luminance adaptation[J]. IEEE Access, 2018, 6: 61277-61286.

[26] Ancuti C O, Ancuti C. Single image dehazing by multi-scale fusion [J]. IEEE Transactions on Image Processing, 2013, 22(8): 3271-3282.

[27] Mertens T, Kautz J, Van Reeth F. Exposure fusion: a simple and practical alternative to high dynamic range photography[J]. Computer Graphics Forum, 2009, 28(1): 161-171.

[28] Joseph J, Sivaraman J, Periyasamy R, et al. An objective method to identify optimum clip-limit and histogram specification of contrast limited adaptive histogram equalization for MR images[J]. Biocybernetics and Biomedical Engineering, 2017, 37(3): 489-497.
[29] Pisano E D, Zong S Q, Hemminger B M, et al. Contrast limited adaptive histogram equalization image processing to improve the detection of simulated spiculations in dense mammograms[J]. Journal of Digital Imaging, 1998, 11(4): 193.
[30] Rodriguez-Molares A, Rindal O M H, D'Hooge J, et al. The generalized contrast-to-noise ratio: a formal definition for lesion detectability[J]. IEEE Transactions on Ultrasonics, Ferroelectrics, and Frequency Control, 2020, 67(4): 745-759.
[31] Akagi M, Nakamura Y, Higaki T, et al. Deep learning reconstruction improves image quality of abdominal ultra-high-resolution CT[J]. European Radiology, 2019, 29(11): 6163-6171.
[32] Zhang A X, He Y H, Wu L G, et al. Tabletop X-ray ghost imaging with ultra-low radiation[J]. Optica, 2018, 5(4): 374-377.
[33] Parsons M S, Sharma A, Hildebolt C. Using correlative properties of neighboring pixels to enhance contrast-to-noise ratio of abnormal hippocampus in patients with intractable epilepsy and mesial temporal sclerosis[J]. Academic Radiology, 2019, 26(4): e1-e8.
[34] Rodgers G, Schulz G, Deyhle H, et al. Optimizing contrast and spatial resolution in hard X-ray tomography of medically relevant tissues[J]. Applied Physics Letters, 2020, 116(2): 023702.
[35] Tao S Z, Rajendran K, Zhou W, et al. Improving iodine contrast to noise ratio using virtual monoenergetic imaging and prior-knowledge-aware iterative denoising (mono-PKAID)[J]. Physics in Medicine and Biology, 2019, 64(10): 105014.

Photographic Image Enhancement for Single-Shot X-Ray Radiograph via Ultrafast Laser

Tang Liping[1,2], Wang Yao[3], Chu Genbai[4], Li Fengxiao[1,2], Wang Liang[3], Zhou Rifeng[1,2*], He Bi[3**]

[1] *ICT Research Center, Key Lab of Optoelectronic Technology and Systems, Ministry of Education, Chongqing University, Chongqing* 400044, *China*;

[2] *Engineering Research Center of Industrial Computed Tomography Nondestructive Testing, Ministry of Education, Chongqing University, Chongqing* 400044, *China*;

[3] *Institute of Chemical Materials, China Academy of Engineering Physics, Mianyang* 621900, *Sichuan, China*;

[4] *Science and Technology on Plasma Physics Laboratory, Laser Fusion Research Center, China Academy of Engineering Physics, Mianyang* 621900, *Sichuan, China*

Abstract

Objective Single-shot X-ray radiograph technology via ultrafast laser can be used to image the internal structure of ultra-high velocity objects with high spatial and temporal resolution, providing a new technical means to observe the internal structure, planarity and other morphological parameters of flyers. However, the wide energy spectrum of high-energy X-rays produced by laser bombardment of the target is accompanied by strong disturbances such as high-energy electrons and scattered rays, which causes great interference to X-ray imaging signal-to-noise ratio and image quality. Besides, the laser pulse width is extremely narrow (picosecond or femtosecond levels) and the data acquisition time of the radiation detector is extremely short, resulting in a low photon count, high quantum statistical noise, and low image signal-to-noise ratio. In addition, the plasma around the flyer makes it more difficult to observe the structure of the flyer, and the image quality is difficult to satisfy the application requirements of accurate observation. Finally, general image enhancement algorithms introduce unnecessary artifacts. In order to better observe and analyze the morphological structure of flyers, a special image enhancement algorithm is needed to improve the image quality.

Methods Aiming at the problems of single-shot X-ray radiograph via ultrafast laser with high background noise interference, low contrast, and difficulties in morphology identification and measurement, an improved histogram equalization image enhancement algorithm based on multi-scale fusion (IHEMF) is proposed in this paper. The conventional CLAHE algorithm uses a fixed clipping threshold, which leads to excessive enhancement of the background region. The IHEMF algorithm modifies the fixed clipping threshold of the CLAHE algorithm to a gradient-dependent parameter. By calculating the horizontal gradient and vertical gradient of each block sub-region in the original image and bringing them into the constructed Gaussian function, adaptive clipping thresholds that can better fit different regional features are obtained. At the same time, in order to avoid the halo phenomenon in the light-dark boundary region, the brightness weight and gradient weight of the original image and the enhanced image by the improved CLAHE algorithm are first calculated, and then the fused images are obtained by pyramid decomposition and reconstruction. When the contrast and shape of the flyer are enhanced, the noise is also amplified. To reduce the effects of plasma and quantum noise in the fused image, block matching 3D (BM3D) denoising algorithm is employed. A three-channel flyer image is obtained by adding pseudo-color to the denoised image in order to obtain better visual effects. In order to verify the effectiveness of the IHEMF algorithm, the enhancement experiments of the static, dynamic and final state images are carried out and the results are compared with those of the commonly used algorithms such as HE, CLAHE, MSR, cl-BHE, ROPE and FCCE.

Results and Discussions We tested the performance of the IHEMF algorithm using static, dynamic and final state images [Figs. 4(a), 5(a) and 6(a)]. The results for three typical images show that the morphology processed by IHEMF algorithm [e.g., Fig. 4(h)] is clearly visible, while other algorithms such as HE, CLAHE, MSR, cl-BHE, ROPE and FCCE [e.g., Figs. 4(b)–4(g)] have little enhancement effect (the material inside the metal cavity cannot be seen). In addition, the images processed by other algorithms have disadvantages such as excessive enhancement in the background area, halo phenomenon at the image edges and strong plasma interference, which are not suitable for observation. IHEMF algorithm reduces the influence of plasma and halos, and the shape of the flyer in the processed image [Figs. 4(h), 5(h) and 6(h)] is clearly visible. The contrast noise ratio (CNR) indicates the ability to distinguish the region of interest (ROI) from the background region, which is used to evaluate the image enhancement effect of the algorithm. The CNR of the images processed by the IHEMF algorithm is significantly improved over the CNR of the original images and the increasing rate is much higher than those of the other algorithms (Table 1), such as HE, CLAHE, MSR, cl-BHE, ROPE and FCCE. Experimental results for three typical images show that the IHEMF algorithm improves the contrast of the ROI and has better enhancement performance compared with other classical image enhancement algorithms.

Conclusions In this paper, we describe an improved histogram equalization image enhancement algorithm combined with multi-scale fusion. The algorithm combines the enhancement characteristics of the improved CLAHE algorithm and the structural retention characteristics of the pyramid fusion algorithm, and the BM3D algorithm is used in order to reduce plasma effects. The research shows that the proposed method can effectively suppress image artifacts and noise (halos and plasma), enhance the contrast of X-ray images, and significantly improve the visual effect. Compared with the original image, the CNR of the image processed by the IHEMF algorithm is significantly improved, and the increasing rate is much higher than those of the other algorithms. The IHEMF algorithm greatly improves the contrast and image quality of the ROI and lays the foundation for accurately obtaining characterization parameters such as internal structure and planarity of the flyer from single-shot X-ray radiograph via ultrafast laser.

Key words ultrafast laser; single-shot X-ray radiograph; image enhancement; multi-scale fusion; histogram equalization